Chapter 25

Detecting Perched Water Bodies Using Surface-seismic Time-lapse Traveltime Tomography

David Gaines[1], Gregory S. Baker[1], Susan S. Hubbard[2], David Watson[3], Scott Brooks[3], and Phil Jardine[4]

Abstract

Applications of seismic time-lapse techniques generally are constrained to large-scale investigations that are associated with petroleum exploration and exploitation. There is growing interest in using geophysical methods to monitor near-surface phenomena, such as fluid flow in fractured or karstic bedrock, hydraulic infiltration, and anthropogenic manipulations during environmental remediation. Previous near-surface geophysical time-lapse studies have focused on electrical or electromagnetic (EM) techniques (including ground-penetrating radar) or borehole methods. To evaluate the utility of surface seismic time-lapse traveltime tomography, we monitor a site through time along a single 2D profile. The objective is to attribute increases in seismic P-wave velocity with the development of perched water bodies in the upper four meters of the subsurface. Our study was conducted in the Y-12 Area of Oak Ridge National Laboratory in Tennessee, U.S.A., in conjunction with a broader multidisciplinary investigation on the fate and transport of contaminants. Because of previous anthropogenic alterations of the site associated with remediation efforts (e.g., replacing as much as 7 m of contaminated soil with poorly sorted limestone gravel fill during construction of a seepage basin cap) the near-surface hydrogeology is extremely heterogeneous and is hypothesized to have a large influence on differential infiltration, contaminant distribution, and contaminant remobilization. The seismic data are processed using a wavepath eikonal traveltime (WET) tomography approach, and a modified trend-analysis technique is applied to remove the larger spatial component associated with geologic variability. The final "residual" velocity-anomaly images are compared with wellbore hydrologic data and error analyses and are used to interpret the presence and geometry of perched water in the shallow subsurface. Our study suggests that velocity estimates obtained from surface-seismic traveltime tomography methods are effective for indicating the spatial and temporal distribution of perched water bodies at the Oak Ridge site in the upper 4 m of the subsurface.

Introduction

We explore the utility of seismic time-lapse P-wave traveltime tomography (STLTT) for monitoring the presence or absence of perched water bodies in the upper 4 m of the subsurface at the S-3 ponds in the Y-12 site of the U.S. Department of Energy (DOE) Oak Ridge Reservation in Oak Ridge, Tennessee. In 2007, DOE established the Oak Ridge Integrated Field-Research Challenge (ORIFRC) to investigate the rates and mechanisms of in situ

[1]*Earth and Planetary Sciences, University of Tennessee, Knoxville, Tennessee, U.S.A. E-mail: dgaines1@utk.edu; gbaker@utk.edu.*
[2]*Earth Sciences Division, Lawrence Berkeley National Laboratory, Berkeley, California, U.S.A. E-mail: sshubbard@lbl.gov.*
[3]*Environmental Sciences Division, Oak Ridge National Laboratory, Oak Ridge, Tennessee, U.S.A. E-mail: watsondb@ornl.gov; brookssc@ornl.gov.*
[4]*Biosystems Engineering and Soil Sciences, University of Tennessee, Knoxville, Tennessee, U.S.A. E-mail: pjardine@tennessee.edu.*

immobilization of contaminants in the subsurface. A subset of this multidisciplinary research includes analyzing geophysical responses to hydrologic properties, because the flux during rainfall events is hypothesized to exert a large influence on contaminant remobilization and distribution. This study focuses on perched water bodies in the upper 4 m of the vadose zone at the ORIFRC, because they are believed to influence the rate and spatial location of hydrologic recharge that impacts deeper contaminated regions.

Research site

The S-3 ponds (Figure 1) were constructed in 1951 for waste-disposal activities. They consist of four unlined ponds ~5 m deep and covering an area of ~120 × 120 m, with a total storage capacity of ~10,000,000 gal (37,854,000 L) for all four ponds (U.S. DOE, 1997). A variety of liquid and sludge wastes composed principally of nitrate, metals, and various radionuclides (e.g., uranium and technetium) is known to have been disposed of in the S-3 ponds (Watson et al., 2005). Total contaminant-mass estimates vary; however, from 1951 to 1983 the ponds received ~2,000,000 gal (7,571,000 L) of liquid waste per year that consisted of condensate mixed with nitric acid and aluminum nitrite in various concentrations (U.S. DOE, 1997). Additional wastes, including sludge from clean-up activities, aerosol cans, and contaminated sediments, were disposed of in the S-3 ponds, but precise mass estimates were not available (U.S. DOE, 1997). The ponds were neutralized and denitrified during 1983–1984, and they were filled and capped in 1988 under the Resource and Conservation Recovery Act (U.S. DOE, 1997). The ponds were unlined, so infiltration and density-driven flow has resulted in an extensive contaminated groundwater plume in the underlying geologic media. That contaminated groundwater has acted as a secondary contaminant source (Watson et al., 2005).

The research site described here is directly adjacent to the former S-3 ponds (in a southwesterly direction) and is oriented perpendicularly to the predominant direction of groundwater flow, parallel to geologic strike (Solomon et al., 1992). The underlying geology (Figure 2) is dominated by the presence of the Nolichucky Shale, a member of the Cambrian Conasauga Group, which dips ~45° to the southeast and strikes N55°E (Hatcher et al., 1992; Watson, et al., 2005). The competent Nolichucky Shale transitions toward the ground surface into a less-competent, weathered bedrock (i.e., saprolite) that retains the fracture and bedding attributes of its parent rock (Watson et al., 2005). The hydrology of the research site is extremely complex as a result of remnant anthropogenic alterations of the site, including as much as 7 m of poorly sorted limestone gravel fill, construction of a cap (causing highly variable water recharge during rainfall events), and construction of a gravel-lined drainage ditch adjacent to the ponds (causing unpredictable surface-water fluxes).

The current conceptual model is that large hydraulic conductivity contrasts between the highly permeable anthropogenic fill and the lower-permeability saprolite, in concert with the preferential recharge of the drainage ditch and impermeable cap, create a saturated perched zone during rainfall events. Water-budget studies have

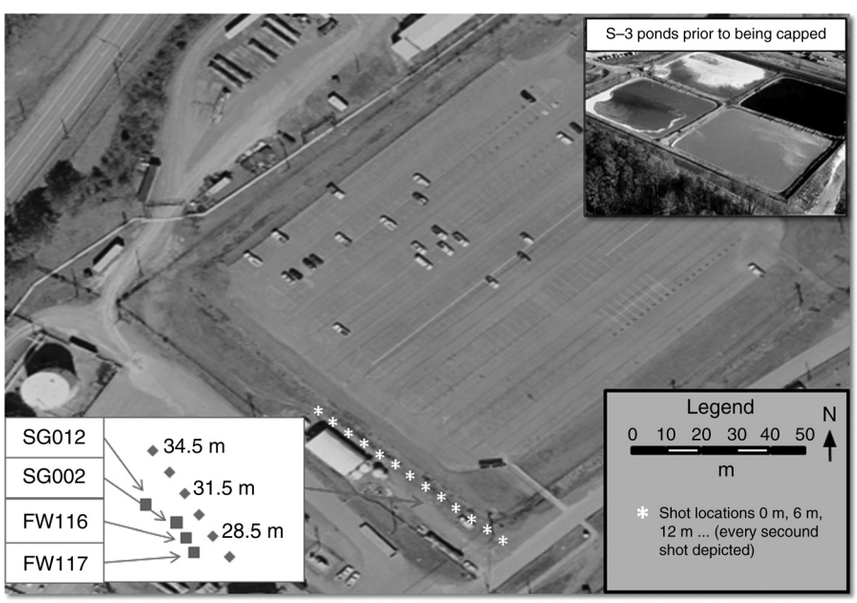

Figure 1. Aerial photo of the S-3 ponds at Y-12 Oak Ridge National Laboratory. The parking lot was constructed on top of the former ponds. Shot locations are indicated on the photo. Well locations and adjacent geophones are depicted in the inset.

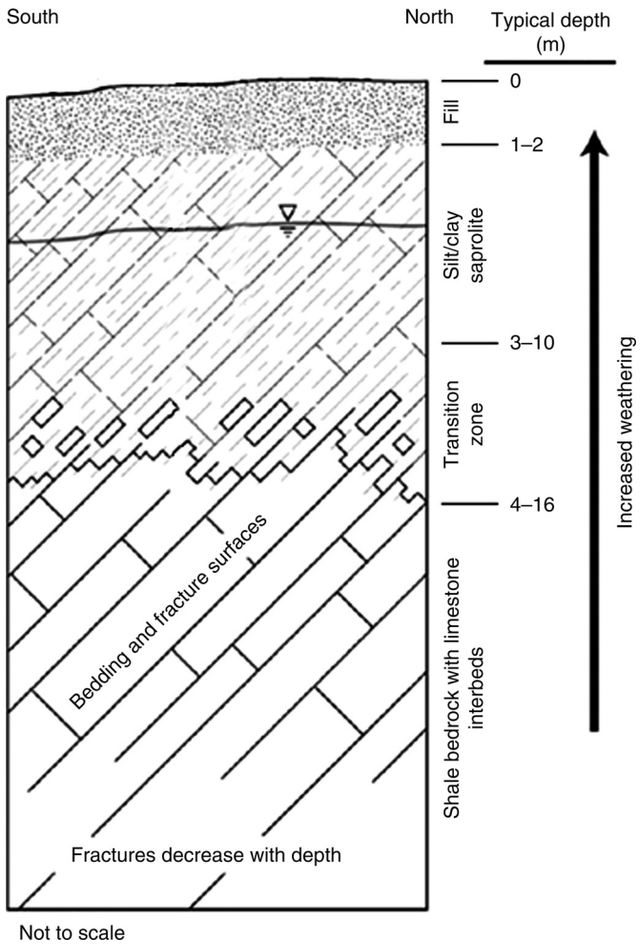

Figure 2. Conceptual model for underlying geology at the ORIFRC. Modified after Watson et al. (2005).

indicated that much of the subsurface flow (~90%) at Oak Ridge takes place in the extreme near-surface (~0.8- to 1.2-m-deep) storm-flow zone (Solomon et al., 1992). At Oak Ridge, this storm-flow zone usually is associated with heavily vegetated areas. That contrasts significantly with the characteristics of the S-3 ponds, where water typically remains ponded in the drainage ditch adjacent to the S-3 ponds for several days after a large rainfall event. The perched water table at the ORIFRC varies but generally is 1–2 m below surface, and it ranges from ~305 m to 307 m above sea level, with ground level ranging from ~307 m to 308 m above sea level. The regional water table is less responsive to infiltration and is 3–5 m below surface (from ~303 to 304 m above sea level). The spatial locations of vertical recharge are affected by the distribution of the perched water bodies. The recharge is important at the ORIFRC because it provides a source of high dissolved-oxygen values and higher-pH water values relative to conditions at depth. Also, the surface water readily mixes and reacts with contaminants.

Previous characterization at ORIFRC

Multiple investigations have been performed at the ORIFRC using seismic techniques (Sheehan et al., 2005b; Watson et al., 2005; Chen et al., 2006). Much of the previous work has focused on characterizing low seismic-velocity zones and has demonstrated the coincidence between those zones and high-hydraulic-conductivity zones. For example, Chen et al. (2006) used joint stochastic inversion of cross-well seismic traveltimes and hydrologic data to estimate the distribution of high-hydraulic-conductivity zones. Beyond the benefits of local characterization of preferential flow paths, their study also demonstrated that a local high-permeability zone exists at depths between 10.5 m and 13.5 m. The existence of that zone has been hypothesized on the basis of surface seismic methods (Sheehan et al., 2005b).

Sheehan et al. (2005b) acquired seismic data in support of research at the Natural and Accelerated Bioremediation Research (NABIR) Field Research Center (FRC), which is the predecessor of the ORIFRC. The seismic data show the existence of a low-velocity zone at depth with very low ray coverage, presumed to indicate a high-hydraulic-permeability conduit, or pathway, in the underlying bedrock (Sheehan et al., 2005b). Although the cavities have not been drilled at the site, a separate anomaly located at the eastern end of Y-12 was located using seismic techniques and confirmed as a mud-filled cavity by driller's logs (Sheehan et al., 2005b). Watson et al. (2005) used coincident 2D surface-seismic and electrical data sets to select the location and depth of investigation for wellbores used in conjunction with a bioremediation study at the ORIFRC. Surface-seismic data were used in conjunction with borehole data to estimate the location of the transition zone between saprolite and competent bedrock as well as to locate probable areas of preferential flow (Watson et al., 2005). The surface electrical data were used to target areas of high electrical conductivity associated with elevated contaminant levels, and then they were integrated with the seismic data on the basis of spatial coincidence between seismically predicted preferential pathways and observed pathways using electrical methods (Watson et al., 2005). In addition, surface ground-penetrating radar was tested at the site to characterize near-surface anomalies, but that was not implemented because of the high electrical conductivity of the surface layers at the site (G. Baker, personal communication, 2007).

Although our work was influenced by Sheehan et al. (2005b), the depth of our investigation is significantly different (i.e., an ~1- to 6-m depth for our investigation). Also, our study focuses on perched water bodies that would appear as high-velocity zones because of presumed complete saturation, rather than on bodies that would appear as low-velocity zones (>10-m depth) because of variation in competency of bedrock or fracture density.

Petrophysical model and error analysis

Conceptually, a change in saturation is expected to affect both density and effective bulk modulus, and consequently the P-wave velocity. The mathematical relationship between density, effective bulk modulus, and saturation has been documented previously (see, e.g., Domenico, 1974; Mavko et al., 1995; Bachrach and Nur, 1998), but it can be divided into a linear and a nonlinear domain (Figure 3). The linear domain is the region above the regional water table (i.e., it is the vadose zone) where a change in P-wave velocity is attributable to replacement of air with water in pore spaces. According to the Gassmann equation, the nonlinear domain is at 99% saturation and greater (i.e., typically at and below the regional water table), and a change in P-wave velocity is attributable to an increase of the effective bulk modulus as a result of fluid interactions. Descriptively, the linear domain is characterized by a gradual decrease in P-wave velocity with increasing saturation levels (i.e., as saturation increases, density increases and velocity decreases), whereas the nonlinear domain exhibits a rapid increase in P-wave velocity at 99–100% saturation. Recent laboratory measurements (George et al., 2009) have suggested that the change in seismic velocity is less abrupt than expected by these theoretical predictions and that seismic P-wave velocity begins to increase before samples are completely saturated. In practice, this effect would introduce additional uncertainty in our measurements because it suggests that velocity increases may result from partial (rather than full) saturation only. However, George et al. (2009) indicate that seismic velocity in their heterogeneous soil mixture begins to increase gradually at <80% saturation, and not until ~90% saturation does seismic velocity begin to increase significantly. In our trend analysis (discussed below), we use a threshold P-wave velocity of 50 m/s, which partially accounts for the limited velocity increase at less than fully saturated levels. Thus, it is presumed that our trend-analysis images map out regions of saturation levels greater than 90% and that these regions indicate the target perched water bodies. Our hypothesis, therefore, is that the development of perched water bodies in the vadose zone will lead to changes in saturation (>90%) that will be detectable through P-wave velocity increases estimated using time-lapse surface-seismic data sets, thereby effectively highlighting the transition between the linear and nonlinear petrophysical model domains.

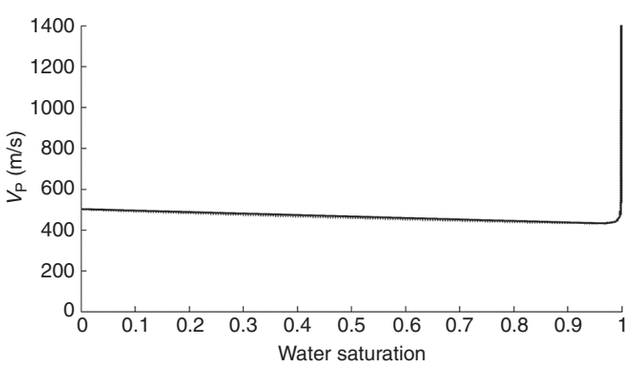

Figure 3. Petrophysical relationship between water saturation and P-wave seismic velocity according to the Gassmann equation.

Sensitivity analyses of near-surface seismic tomography indicate the difficulty in accurately measuring subsurface velocities and provide a general estimate of the reliability of the tomography algorithm (Sheehan et al., 2005a; Hiltunen et al., 2007). The algorithm employed in this investigation is the wavepath eikonal traveltime (WET) algorithm, which is designed to account partially for wavepath effects by back-projecting traveltime residuals using a source weighting function (Schuster and Quintus-Bosz, 1993). The source weighting function in the WET algorithm is a gradient function that depends on the traveltime residuals, source and receiver locations, the slowness model, and geometrical spreading terms. For a Ricker wavelet with a given peak frequency, the source weighting function is evaluated at all points in the traveltime grid, and the model is updated by distributing the residuals according to results of the source weighting function.

The generalized processing workflow includes picking first-arrival times for all sources and receivers, generating an initial slowness model and solving the eikonal equation (see Lecomte et al., 2000), then updating the model and continuing iteration until convergence. This is a computationally efficient way of partially accounting for "fat" rays, or the Fresnel volume associated with a propagating wave. Sheehan et al. (2005a) tested the WET algorithm using various synthetic models and found that the average rms error associated with a specific inversion relative to the true model was ~600 m/s. In most cases, the areas for which the rms error was calculated exhibited velocities

ranging from 1000 m/s to 3000 m/s, although the area sampled and its associated rms error varied depending on initial synthetic model. As Sheehan et al. (2005b) stated, the rms error could be reduced significantly by altering smoothing parameters; however, this may result in the introduction of artifacts resulting from noise and inconsistent first-arrival picks. Although the tomographic images associated with this study are coupled via a shared initial model that is updated with minimal smoothing, they are wholly separate data sets that yield qualitatively similar images when processed independently with full smoothing. If successive STLTT data independently show an area of increased velocity above the regional water table, it is likely the anomaly is not an artifact caused by processing parameters.

If a 600-m/s rms error is accepted as the standard error associated with WET tomographic inversions, many shallow features, including near-surface seismic velocity features caused by variations in saturation, would be undetermined because of the expected error in velocity measurements. However, previous work has demonstrated the sensitivity of high-frequency seismic waves to small near-surface velocity variations. Additionally, shallow water-table reflections and refractions have been imaged at depths of <2 m (Baker et al., 1999a; Baker et al., 1999b; Baker et al., 2000a) that are sensitive to partial saturation (Birkelo et al., 1987; Bachrach and Nur, 1998; Baker et al., 2000b) and have been used successfully in mapping near-surface hydrostratigraphic reflectors (Lankston, 1989; Baker et al., 1999a; Baker et al., 2002; Garambois et al., 2002).

Methodology and Results

The methodology for data acquisition is indistinguishable from many typical near-surface seismic-refraction surveys. However, the assumption that all first arrivals are to the result of refracted head waves may not be valid, so we avoid terminology involving "refraction" and instead consider "first arrivals" more appropriate. The seismic data presented here were collected during October and November 2007 and represent a selected time-slice during a period of increased rainfall. Hydrologic data, including precipitation, elevation of the regional water table, and elevation of the perched water table, were collected over the same time period and are nearly continuous at 15-minute intervals. However, occasional gaps in coverage exist where equipment malfunctioned, as well as artifacts whereby the measured groundwater table rapidly oscillates.

Seismic data acquisition

Beginning in October 2007, we repeatedly collected coincident seismic P-wave traveltime 2D profiles and wellbore hydrologic data at the ORIFRC in order to monitor the development of perched water bodies that resulted from recharge. Each seismic profile is identical in acquisition geometry and spatial location and represents a time-dependent P-wave velocity image of the subsurface at the ORIFRC. The data used in the error analysis were collected during October 2007. The data for the time-lapse study of the perched water body were acquired during November 2007 and depict a period of increased rainfall. Seismic data acquisition was accomplished using two 24-channel Geometrics Geodes with 100-Hz vertical geophones located at 1.5-m intervals along the profile. The profile extends perpendicularly to geologic strike and parallel to the southwestern edge of the former S-3 ponds (see Figure 1). We stacked and recorded multiple seismic shots at each source location, using a conventional 2.2-kg (5-lb) sledgehammer and plate. The source-station interval was 3 m.

Geophones were removed and replaced for each acquisition period, and to maintain similarity between surveys, semipermanent plastic stakes were emplaced at 1.5-m intervals along the profile. During subsequent surveys, the semipermanent stakes were used to identify previous geophone locations, thereby ensuring minimal error caused by variation of geophone placements between surveys. Shot locations were directly adjacent to geophone locations and were similarly reproducible. The maximum error for relocating geophones was $\pm$ 5 cm; however, the positioning often was identical. To limit the effect of variable acquisition parameters or processing, data were not manipulated in the field (i.e., filters were not applied, and minimal preamp gain was applied). Because of anthropogenic noise outside the control of the experiment, stack numbers varied between acquisition periods. However, because we are not comparing amplitude but rather first-arrival times, we do not expect that variation to significantly affect first-arrival pick times or the subsequent tomographic inversions.

Hydrologic data acquisition

The site is extremely well instrumented, and a variety of hydrologic information has been collected at the ORIFRC. We chose to use four wells in this study to provide ground truthing, on the basis of their proximity to the seismic profile and because they provide nearly continuous information for the period of November 2007. The hydrologic wells are offset perpendicularly from the

profile by approximately 0.5 to 1 m and are located at positions that correspond to the 26- to 30-m points on the profiles. The wells are screened at different intervals, depending on their original purpose (i.e., FW116 and FW117 are screened at greater depth to measure the regional water table, whereas SG002 and SG012 are shallow-water-table wells designed to monitor the known perched water table). Water-table-elevation measurements were acquired at 15-minute intervals via semipermanent pressure transducers. Precipitation data also were acquired at 15-minute intervals via a rain gauge installed on site, and a secondary rain gauge located at the west end of the Y-12 plant, approximately 1 km away from the research site, is used during a gap in coverage. The water-table-elevation measurements provide information regarding the top of the perched water table and the regional water table, and although they are point measurements they presumably provide estimates that can be extrapolated laterally to some degree. Additionally, it is important to clarify that the wells are not perfectly coincident with the seismic profiles, because there is some lateral offset and some variation may be expected.

Seismic data

The tomographic inversion results associated with the October 2007 site-specific error analysis are presented in Figure 4, and the inversion results used to delineate the perched water body from November 2007 are presented in Figure 5. An example of typical data quality and associated first-arrival picks from November 2, 2007 is shown in Figure 6. The corresponding raypaths are presented in Figures 7 and 8, respectively. The inversion results in Figure 4 depict three separate seismic surveys at the same location on the same day, and the corresponding raypaths are shown in Figure 7. The inversion results in Figure 5 are from data collected during November 2007, and the raypaths associated with these images are presented in Figure 8. In each case, the inversion results are ordered vertically, with the earliest survey located at the top. For both the error-analysis data and the November 2007 data, the raypath and inversion results are related by their component (i.e., the inversion results in Figure 4a correlate to the raypaths shown in Figure 7a). Both sets of data were processed using the WET algorithm (Schuster and Quintus-Bosz, 1993), employing commercially available software (Rayfract, Intelligent Resources Inc.). Data quality varied throughout each profile; however, in general, accurate first-arrival picks were made out to ~48-m shot-receiver offsets. Unfavorable noise conditions (e.g., traffic noise,

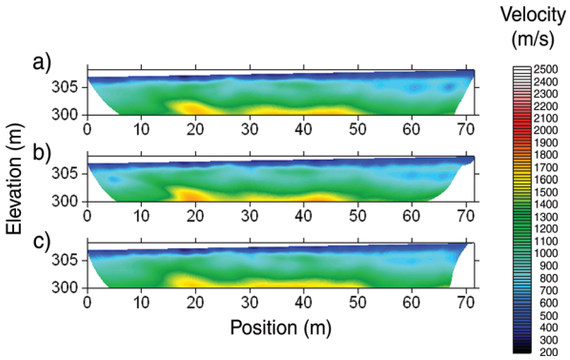

Figure 4. Repeated 2D profiles acquired on the same day in October 2007 with no precipitation between acquisitions. The lettering corresponds to (a) initial profile, (b) profile acquired 2 hours after initial profile, (c) profile acquired 4 hours after initial profile.

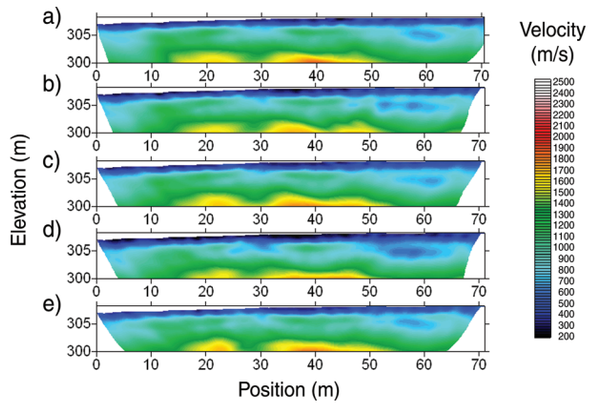

Figure 5. Seismic 2D profiles at the ORIFRC site, acquired on different days in November 2007. The lettering corresponds to profiles acquired on (a) November 2, 2007, (b) November 7, 2007, (c) November 9, 2007, (d) November 16, 2007, and (e) November 21, 2007.

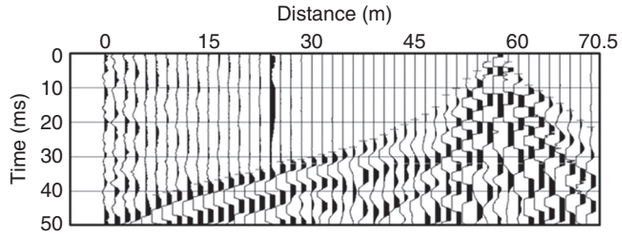

Figure 6. Seismic data acquired at the ORIFRC site on November 2, 2007. There are 48 channels spaced at 1.5-m increments, from 0 to 70.5 m. The source was located at 57 m. The seismic data are normalized and clipped to prevent adjacent traces from overlapping.

generators) occasionally resulted in degraded signal-to-noise at the outer offsets, but this principally affects only the resolved depth of the tomograms and not the resolution at the shallowest levels of the tomograms. The frequency range of the data sets is relatively high, with an average peak frequency of ~100 Hz for most shot gathers.

To couple each profile to a baseline, the output velocity tomogram of the inverted baseline data set is used as the initial velocity model for subsequent profiles (see Sarkar et al., 2003). The baseline data set for both the error analysis and the perched-water-body study is the first profile presented in Figures 4 and 5, respectively. Although it is possible to invert traveltime differences, previous studies suggest that assumptions regarding straight rays are required (Day-Lewis et al., 2002), which is not applicable for our experiment. In addition, traveltime differences likely are a function of changes in ray coverage and in velocity, implying that at the near-surface, differences between seismic surveys would not correlate spatially because of changes in raypaths. Thus, the alternative methodology of coupling profiles via an inverted baseline data set is adopted. Care was taken to begin both the time-lapse survey and the error-analysis survey during a lull in precipitation, to avoid abnormal starting conditions (i.e., no precipitation immediately preceding the profile).

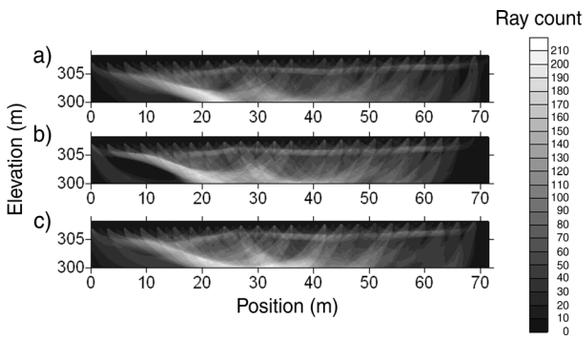

Figure 7. Ray tracing for repeated profiles acquired on the same day in October 2007, with no precipitation between acquisitions. The lettering corresponds to: (a) initial profile, (b) profile acquired 2 hours after the initial profile, (c) profile acquired 4 hours after the initial profile.

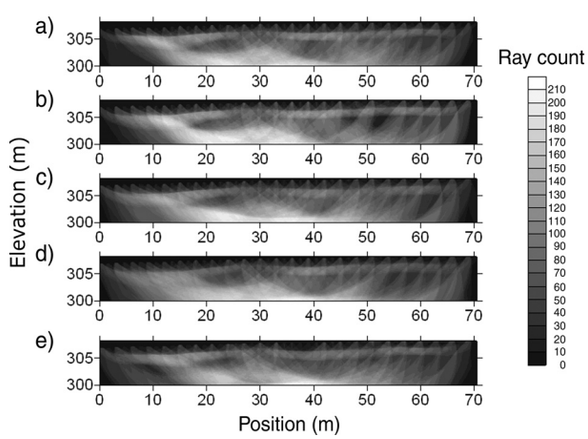

Figure 8. Ray tracing for profiles at the ORIFRC site, acquired on different days in November 2007. The lettering corresponds to profiles acquired on: (a) November 2, 2007, (b) November 7, 2007, (c) November 9, 2007, (d) November 16, 2007, and (e) November 21, 2007.

Hydrologic data

The water-level and precipitation data are displayed in Figure 9 and represent the automated acquisition during November 2007. There was a gap in coverage from November 17 through November 21, and ancillary rain-gauge data

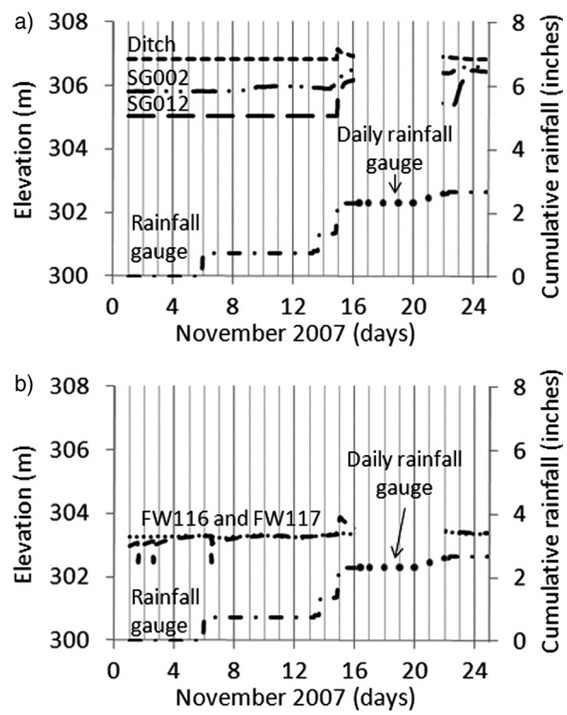

Figure 9. Hydrologic data acquired at the ORIFRC during November 2007. The left axis is a point measurement of the elevation of the water table in the wells, and the right axis is cumulative precipitation at the ORIFRC. (a) The shallow wells and ditch water levels, and (b) the regional water table. Precipitation includes both the rainfall gauge at the site and the daily measurements from a separate location during a period in which no data were collected at the S-3 ponds.

from the aforementioned station (∼1 km away) are used to fill this gap. The gap in hydrologic coverage means that the borehole measurements associated with the tomogram on November 21 actually were acquired on November 22, and the lag between seismic measurement and hydrologic measurement is ∼12 hours.

Discussion

We first address the expected error and resolution of the tomographic inversions. A site-specific error analysis is performed prior to the collection of time-lapse profiles because of the expected difficulty in obtaining accurate velocity estimates for a near-surface, variably saturated perched water table. In addition to the site-specific error analysis, checkerboard resolution tests are performed for the baseline profiles of both the error analysis and the time-lapse study. Following discussion of the resolution and error analysis, we present the trend-analysis approach used to image the perched water table, and then we integrate the hydrologic data with the trend analysis.

Inversion resolution

Inversion quality can be assessed by numerous different metrics, and we will present several metrics used on the October 2007 data. The typical mean unsigned error between modeled and picked times after processing was <1 ms (∼0.3 ms). Maximum error between the observed and modeled traveltimes was ∼2 ms, although it is expected that that error would be minimized in an iterative tomographic reconstruction. Ray coverage for the two data sets is variable (see Figures 7 and 8) but provides a general estimate of how well the model is constrained at specific grid points (see Zelt et al., 2006).

An additional technique for estimating tomographic-inversion sensitivity is to use a checkerboard resolution test (Humphreys and Clayton, 1988). A checkerboard test is performed in several steps, the first of which is inversion of the synthetic traveltimes of the tomogram to be tested (Figure 10a). A checkerboard pattern of velocity perturbations (10% of maximum at any grid node) is added to the inversion of the synthetic traveltimes (Figure 10b), and synthetic traveltimes are generated again for the updated model. The updated model is inverted again (Figure 10c), and the residuals between this final inversion and the initial model (the model in 10b) are calculated. These residuals are scaled from −100% to 100%, relative to the initial velocity perturbation, and are plotted for visual inspection (Figure 10d). The results of the checkerboard are a quantitative indicator of model resolution, and maintaining the shape and amplitude of the checkerboard pattern indicates the resolution of the tomogram (see Zhao et al., 1992; Zollo et al., 2002).

The checkerboard resolution test is performed for the initial profile used in the error analysis (October 2007 data; Figure 10) and for the time-lapse study (November 2007 data; Figure 11) to establish the resolution of the model. For the error analysis (Figure 10d), the checkerboard test indicates that the center of the profile is satisfactorily resolved and an expected loss of resolution occurs at either end of the profile. The checkerboard test for the time-lapse data (Figure 11d) shows greater model resolution, although some lateral and vertical smearing is visible in the center of the image. This smearing is presumed to represent the perched water table, because its location in the image is coincident with the presumed location of the perched water body.

Velocity error analysis

To resolve the incongruity between high rms error and demonstrated seismic sensitivity to near-surface saturated zones, an intermediate interpretation was chosen so that

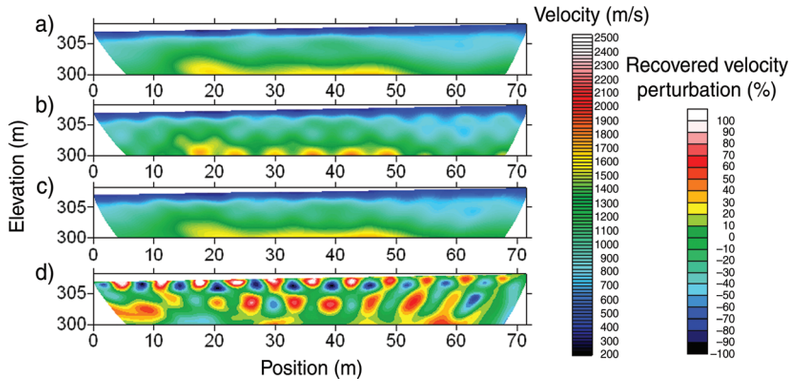

Figure 10. Checkerboard resolution test results for the baseline profile in the error analysis. The lettering corresponds to (a) results of inversion of synthetic data, (b) addition of sinusoidal velocity perturbation, (c) inversion of synthetic traveltimes of perturbed model, and (d) residual after subtracting profile A from profile C following normalization.

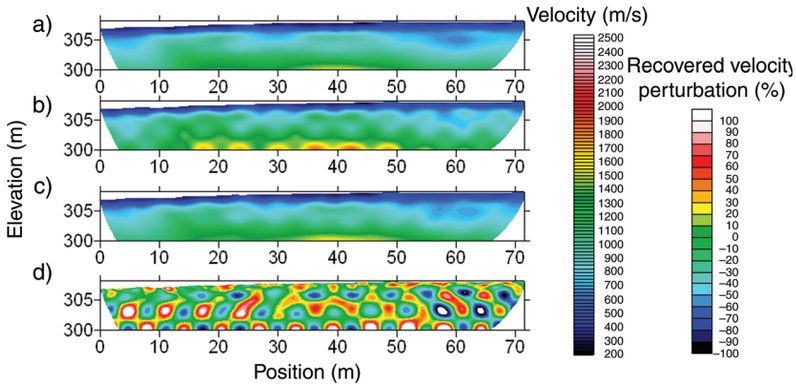

Figure 11. Checkerboard resolution test results for the baseline profile in the time-lapse data set. The lettering corresponds to (a) results of inversion of synthetic data, (b) addition of sinusoidal velocity perturbation, (c) inversion of synthetic traveltimes of perturbed model, and (d) residual after subtracting profile A from profile C following normalization.

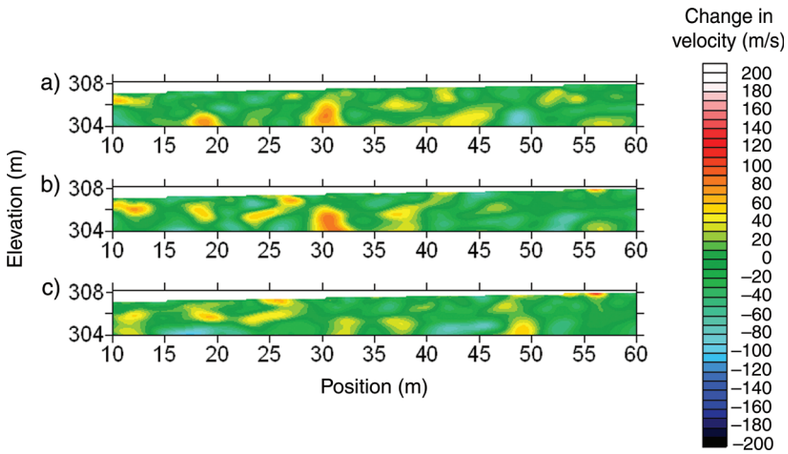

Figure 12. The result of differencing between the error analysis profiles. (The profiles are depicted in Figure 4 before subtraction.) The lettering corresponds to (a) initial profile minus the profile acquired 2 hours after the initial profile, (b) initial profile minus the profile acquired 4 hours after the initial profile, and (c) the profile acquired 2 hours after the initial profile minus the profile acquired 4 hours after the initial profile.

precise velocity estimates were not necessary. In other words, determining whether the velocity estimates are correct relative to the true model was considered unimportant, as long as they are represented consistently. The results of the checkerboard resolution test imply that the model is resolved satisfactorily in the region of interest (i.e., at the suspected location of the perched water bodies), indicating that the inverted model is reliable (see Zhao et al., 1992; Zollo et al., 2002).

To understand how velocity would change between surveys because of acquisition or inconsistent first-arrival time picks, a site-specific empirical analysis of error was performed at the ORIFRC by acquiring three surveys on the same day, with no precipitation, under the assumption that site conditions are static at that time scale. The inverted profiles (Figure 4) show very little variation of velocity in the vadose zone, although some variations are evident at depth. By taking the difference of the profiles, we can determine the quantitative change in measured velocity between surveys (Figure 12). Although profiles B and C are coupled to profile A in Figure 12, all three tomograms are presented as being equally valid initially, and thus the differences between each are calculated. The differences in the images are dominated by specific anomalous regions with a maximum magnitude of $\sim$83 m/s velocity for profile A (Figure 12a), $\sim$89 m/s for profile B (Figure 12b), and $\sim$108 m/s for profile C (Figure 12c). The rms error is 27 m/s for profile A, 29 m/s for profile B, and 28 m/s for profile C, although Figure 12 illustrates that most of the deviations are localized rather than averaged over the entire profile. Qualitatively, the profiles appear similar in the vadose zone and show some variation at depth. Thus, although there is clearly error in repeatability because of differences in first-arrival picks, acquisition, or processing artifacts, the error is qualitatively minimal in the target area within the vadose zone. It is possible that increased smoothing parameters would decrease the observed differences between profiles; however, the differences are negligible for a qualitative interpretation. As stated, much of the error is the result of specific anomalous regions and is not distributed broadly throughout the tomograms.

Trend-analysis approach

To distinguish the perched water table visually, we explored the use of data differencing and trend analysis. Assuming an invariant background, the difference between two profiles would produce an image of time-variant changes (see Lumley, 2001), and the corresponding difference between two time-invariant profiles would be a homogeneous image. The observed differences (seen in Figure 12) are not homogeneous, thereby indicating the degree of difficulty in replication of surveys and processing. Although these differences are not significant for a qualitative interpretation, they complicated a quantitative, differencing approach.

As an alternative, trend surface analysis was investigated to delimit the spatial extent of the perched water table. Qualitatively, trend surface analysis is the process of separating data into a "regional" component and a "local" component (Davis, 2002). At the ORIFRC, the subsurface is heterogeneous, but the approximation at the near surface is that velocity increases with depth and that the regional component (tens of meters in scale) mirrors this trend. The local component (meter or submeter in scale) is the perched water table, which is an anomalous high-velocity zone above the regional water table. Trend surface analysis is similar to differencing, in that the regional component is subtracted from the image. However, the final product is read more intuitively as an image of the perched water table, compared with subtraction between profiles.

The typical methodology for separating the regional and local components in trend surface analysis is to fit polynomial functions to the data and to inspect the residuals (e.g., Davis, 2002; Evenick et al., 2008). This approach is similar functionally to previous work involving tunnel and near-surface velocity-anomaly detection (e.g., Belfer et al., 1998), but in this case, the background model is derived by using the horizontal average of the Delta-*t*-*V* inversion (Gebrande and Miller, 1985). The resulting images (Figures 13 and 14) of the positive difference between the regional model and the local component indicate the presence of an anomaly above the regional water table. The trend-analysis images in Figure 13 are derived from the error-analysis data (Figure 4). The initial profile (Figure 4a) is not used here because it is a baseline profile, thus Figure 4b and 4c correlates to Figure 13a and 13b, respectively. The trend-analysis images in Figure 14 are derived from the data acquired in November 2007 (Figure 5). Similarly to the error-analysis data, the initial profile (Figure 5a) is not used for the trend analysis, and Figure 5b, 5c, 5d, and 5e correlates to Figure 14a, 14b, 14c, and 14d, respectively.

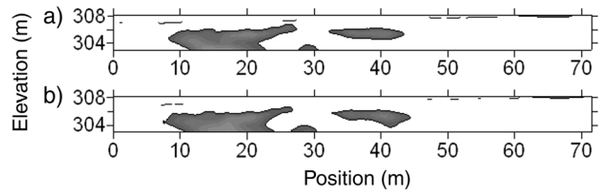

Figure 13. Trend-analysis images highlighting positive seismic-velocity zones greater than 50 m/s for the error-analysis profiles. The images are constructed by subtracting the regional velocity model from the profiles shown in Figure 4. (a) Image that corresponds to Figure 4b and is the profile acquired 2 hours after the initial profile. (b) Image corresponds to Figure 4c and is the profile acquired 4 hours after the initial profile.

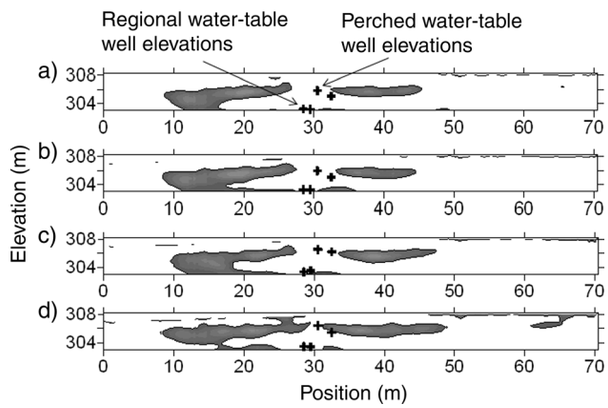

Figure 14. Trend-analysis images highlighting positive seismic-velocity zones greater than 50 m/s for the error-analysis profiles. The images are constructed by subtracting the regional velocity model from the profiles shown in Figure 5. Hydrologic data are overlain on the trend-analysis images using information from Figure 9. (a) Image that corresponds to Figure 5b and was acquired on November 7, 2007. (b) Image that corresponds to Figure 5c and was acquired on November 9, 2007. (c) Image that corresponds to Figure 5d and was acquired on November 16, 2007. (d) Image that corresponds to Figure 5e and was acquired on November 21, 2007.

The maximum magnitude for the error-analysis value is ~100 m/s, and the expected change in seismic velocity from unsaturated to saturated loosely consolidated soils is significantly higher (i.e., ~700 m/s), on the basis of the petrophysical relationship shown in Figure 3. The difference images are generated by subtracting the regional component from the local component and are mapped showing seismic velocities greater than 50 m/s (Figures 13 and 14). The 50 m/s threshold is chosen to account for error in

seismic-velocity measurements and the gradual increase in seismic velocity as a result of the high partial saturations discussed previously. As stated earlier, the maximum error magnitude in the error analysis was ~100 m/s; however, it was believed that this was confined to anomalous zones outside of the target area, and preference was given to maintaining the signal at the expense of possible noise sources.

Integration of trend-analysis data with hydrologic data

The perched water bodies are interpreted as regions of higher velocity located above the regional water table and are identifiable visibly at elevations of ~305 m along the profile (see Figure 5), at approximately 1–2 m below the ground surface. Independent hydrologic point measurements (Figure 14) suggest that this interpretation of the perched water table is reasonable because the two shallow wells indicate an elevated water table at the same depth, ± 0.5 m. The hydrologic point measurements of the perched water table measure the elevation of the top of the water table, which is presumed to have some spatial extent around the well. Thus, the gap in the perched water table in the vicinity of the hydrologic wells, as seen on the tomograms, is not expected. It is possible that the perched water table is thin vertically in this region and that infiltrating water preferentially drains laterally in either direction from the wells. Alternatively, the installation or presence of the hydrologic wells may affect acquisition and perched-water drainage. From direct observation at the site, there is a change in fill characteristics in this region, possibly as a result of initial installation of the boreholes.

Although the perched water table and regional water table are separate phenomena, there are regions in which the tomograms are unable to differentiate between the two. Overlaying the hydrologic data on the trend-analysis images (Figure 14) indicates a separate issue, namely that the velocity anomalies appear to be slightly above the top of the perched water table in many of the images. This disagrees fundamentally with previous findings by Bachrach and Nur (1998), who observed a decrease in velocity as a result of partial saturation of beach sand and the theoretical predictions. A reasonable interpretation, assuming perfect accuracy of the hydrologic data, is that the seismic images are shifted or have a vertical error of approximately ± 1 m. Alternatively, because there are small-scale fluctuations in the measured elevations of the perched water table between the two shallow groundwater wells SG002 and SG012, and SG012 is located at a greater distance from the profile and ditch (Figure 1), the tomograms could be representing the location of the perched water body accurately at the exact location of the profile. In this case, the wells indicate that the perched water table decreases in vertical extent, away from the S-3 ponds. This interpretation is favored, because SG002 is located directly adjacent to the profile whereas SG012 is offset by a larger distance, and SG002 measurements coincide with the top of the observed anomaly.

Regardless of the actual interpretation, it seems reasonable to conclude, on the basis of the measured elevations of the perched water body and the trend-analysis images, that the perched water body is imaged partially or wholly. Although the existence of the perched water table already was known, previously the spatial distribution of the perched zone was bounded only loosely. Additionally, although it was known that the perched water responded to rainfall events, the extent of that influence was unknown previously. Thus, as an initial interpretation, the trend-analysis images bound the vertical extent of the perched water body, assuming that the measured elevations at SG012 represent either a grading out or a change in elevation of the perched water body. The elevations at SG002 are representative of the perched water body at the profile itself, and SG012 represents the horizontal thinning out of the perched water body. The extent of the perched water body is defined only loosely toward the southern end of the profile (i.e., it extends approximately 0–10 m), because resolution tests indicate a lack of coverage.

The trend-analysis images (e.g., Figure 14) exhibit general similarity in the positions of the anomalies, although the dimensions are shown to change in time, particularly for the anomaly centered at the 40-m position. The current hypothesis is that infiltration and rainfall events cause the perched water table to expand in size laterally and vertically. Subsequent to rainfall events, the perched water table decreases in size and reequilibrates to its nominal configuration. The measured hydrologic data (see Figure 9) tentatively support this hypothesis, because water-table measurements in SG012 and SG002 show an increase in elevation after a rainfall event between 14 and 15 November and subsequently a gradual return to a lower elevation. The time between acquisition of a survey and the end of the previous rainfall event supports this hypothesis. For the initial two trend-analysis images (profiles B and C, seen in Figure 14a and b, respectively), the previous rainfall event (of ~0.74 in or 1.88 cm of precipitation) ended on November 5. The lag between the times at which the surveys were collected was approximately 22 hours (~1 day) for profile B (Figure 14a), and approximately 70 hours (~3 days) for profile C

(Figure 14b). Quantitatively, calculations show that the area of the mapped anomaly centered at position 40 m in Figure 14 decreased from $\sim$15 m^2 to 14 m^2 between profiles B and C (Figure 14a and b, respectively). The trend-analysis images show negligible qualitative differences between these two images, although the anomaly centered at the position of $\sim$40 m exhibits some lateral variation. The anomaly in profile C (Figure 14b) is shown to gradually shrink laterally in comparison with profile B (Figure 14a). Hydrologic information (see Figure 9) indicates no vertical increase in depth to the perched water table after the rainfall event. The third profile (profile D, Figure 14c) was acquired approximately 49 hours (2 days) after a prolonged rainfall event on November 14 to November 15 ($\sim$1.4 in or 3.56 cm of precipitation). The perched water table in profile C (Figure 14b) is inflated vertically at the anomaly centered at the position of 40 m, although the anomaly located at 10–28 m exhibits less continuity. Calculations show the areal extent of the mapped anomaly at position 40 m to be $\sim$18 m^2. The vertical increase in groundwater elevation in the trend-analysis image is presumed to be real and mirrors the elevated water-table measurements at SG012. This indicates that the perched water table, which normally thins or grades out away from the S-3 ponds, is increasing vertically. Finally, the fourth profile (profile E, Figure 14d) was acquired on the same day as the rainfall event on November 21. The well information for this profile is from November 22, because no well data were collected during this period. The approximate lag between seismic measurements and hydrologic measurements is 11 hours (one-half day). A separate rain gauge located at the Y-12 plant indicated precipitation during that time, with a precipitation amount listed as $\sim$0.3 in (0.76 cm) of rain. The top of the trend-analysis image correlates with the measured groundwater elevation at SG002, but SG012 again is measured below the anomaly. Quantitatively, the areal extent of the perched water body centered at the 40-m position is 25 m^2. In this case, the hydrologic data indicate that the perched water body thins, or grades out, away from the S-3 ponds. The lateral extent of the anomaly is significantly greater here relative to previous profiles and is presumed to indicate the relative timing between precipitation and acquisition.

Conclusions

We have investigated the application of seismic P-wave time-lapse traveltime tomography (STLTT) for monitoring the presence or absence of perched water bodies in the vadose zone within 4 m of the subsurface. Comprehensive site-specific error analyses indicate that perched water would be within detection limits. The cutoff velocity of our experiment whereby perched water is considered "detected" is 50 m/s, on the basis of both the expected petrophysical relationship (see Figure 3) and subsequent error and resolution analysis specific to the site. On the basis of well measurements that are indicative of the perched water body thinning or pinching out away from the S-3 ponds, the trend-analysis images have submeter accuracy to the measured tops of the perched water bodies. The horizontal resolution is less clearly defined (because of the lack of available well coverage). However, because of the hydrologic complexity and lateral variability at the site, it is not unreasonable to assume that the trend-analysis images (Figure 14) are correct as a first approximation.

Our results have the direct impact that the existing comprehensive hydrologic model for the S-3 ponds region of Y-12 at Oak Ridge National Laboratory — used for evaluating remediation efforts and assessing long-term hazards — will be modified to include heterogeneous infiltration pathways. The hydrologic model for the S-3 ponds area previously represented the surface-water recharge in the vicinity of the secondary-contaminant source as a line source parallel to the edge of the ponds along the drainage ditch, in the region directly adjacent to our 2D seismic profiles. In future iterations of the model, the long line source will be modified and the dominant surface recharge will be characterized instead by several shorter line segments that represent regions of increased infiltration located between the identified perched water bodies. Those regions are based on the correlation lengths mapped out in our time-lapse experiment.

Our investigation indicates that seismic tomography can be used as a high-resolution geophysical tool for monitoring near-surface vadose-zone fluid transport. In this case, perched water bodies within 4 m of the subsurface are identified as high-velocity anomalies because of the expected petrophysical relationship at high levels of saturation ($>$90%). Future research will focus also on identifying time-varying changeability in partially saturated regions through corresponding low-velocity anomalies that are representative of regions having increased but $<$80% saturation, where density changes dominate.

Acknowledgments

Funding for this study was provided by the U.S. Department of Energy, Biological and Environmental Research Program, as part of the Oak Ridge National Laboratory Integrated Field Research Center project (UT-B 4000059241), and by the Jones/Bibee Endowment at the University of Tennessee.

References

Bachrach, R., and A. Nur, 1998, High-resolution shallow-seismic experiments in sand, Part I: Water table, fluid flow, and saturation: Geophysics, **63**, 1225–1233.

Baker, G. S., C. Schmeissner, D. W. Steeples, and R. G. Plumb, 1999a, Seismic reflections from depths of less than two meters: Geophysical Research Letters, **26**, 279–282.

Baker, G. S., D. W. Steeples, and C. Schmeissner, 1999b, In-situ, high-frequency P-wave velocity measurements within 1m of the earth's surface: Geophysics, **64**, 323–325.

———, 2002, The effect of seasonal soil-moisture conditions on near-surface seismic reflection data quality: First Break, **20**, no. 1, 35–41.

Baker, G. S., D. W. Steeples, C. Schmeissner, and K. T. Spikes, 2000a, Source-dependent frequency content of ultrashallow seismic reflection data: Bulletin of the Seismological Society of America, **90**, no. 2, 494–499.

———, 2000b, Ultrashallow seismic reflection monitoring of seasonal fluctuations in the water table: Environmental and Engineering Geoscience, **6**, no. 3, 271–277.

Belfer, I., I. Bruner, S. Keydar, A. Kravtsov, and E. Landa, 1998, Detection of shallow objects using refracted and diffracted seismic waves: Journal of Applied Geophysics, **38**, 155–168.

Birkelo, B. A., D. W. Steeples, R. D. Miller, and M. Sophocleous, 1987, Seismic reflection study of a shallow aquifer during a pumping test: Ground Water, **25**, 703–709.

Chen, J., S. Hubbard, J. Peterson, K. Williams, M. Fienen, P. Jardine, and D. Watson, 2006, Development of a joint hydrogeophysical inversion approach and application to a contaminated fractured aquifer: Water Resources Research, **42**, no. 6, W06425.

Davis, J. C., 2002, Statistics and data analysis in geology: John Wiley & Sons.

Day-Lewis, F. D., J. M. Harris, and S. M. Gorelick, 2002, Time-lapse inversion of crosswell radar data: Geophysics, **67**, 1740–1752.

Domenico, S. N., 1974, Effect of water saturation on seismic reflectivity of sand reservoirs encased in shale: Geophysics, **39**, 759–769.

Evenick, J. C., R. D. Hatcher, and G. S. Baker, 2008, Trend surface residual anomaly mapping and well data may be underutilized combo: Oil & Gas Journal, **106**, no. 4, 35–42.

Garambois, S., P. Senechal, and H. Perroud, 2002, On the use of combined geophysical methods to assess water content and water conductivity of near-surface formations: Journal of Hydrology, **259**, 32–48.

Gebrande, H., H. Miller, 1985, Refraction seismology, *in* F. Bender ed., Applied geosciences II: Ferdinand Enke Publishing House, 226–260.

George, L. A., M. M. Dewoolkar, and D. Znidarcic, 2009, Simultaneous laboratory measurement of acoustic and hydraulic properties of unsaturated soils: Vadose Zone Journal, **8**, no. 3, 633–642.

Hatcher, R. D., P. J. Lemiszki, R. B. Dreier, R. H. Ketelle, R. R. Lee, D. A. Leitzke, W. M. McMaster, J. L. Foreman, and S. Y. Lee, 1992, Status report on the geology of the Oak Ridge Reservation: Environmental Science Division Publication, no. 3860, ORNL/TM-12074.

Hiltunen, D. R., N. Hudyma, T. P. Quigley, and C. Samakur, 2007, Ground proving three seismic refraction tomography programs: Transportation Research Record, **2016,** 110–120.

Humphreys, E., and R. W. Clayton, 1988, Adaptation of back projection tomography to seismic travel time problems: Journal of Geophysical Research — Solid Earth and Planets, **93**, 1073–1085.

Lankston, R. W., 1989, The seismic refraction method: A viable tool for mapping shallow targets into the 1990s: Geophysics, **54**, 1535–1542.

Lecomte, I., H. Gjoystdal, A. Dahle, and O. C. Pedersen, 2000, Improving modelling and inversion in refraction seismics with a first-order Eikonal solver: Geophysical Prospecting, **48**, 437–454.

Lumley, D. E., 2001, Time-lapse seismic reservoir monitoring: Geophysics, **66**, 50–53.

Mavko, G., C. Chan, and T. Mukerji, 1995, Fluid substitution — Estimating changes in V-P without knowing V-S: Geophysics, **60**, 1750–1755.

Sarkar, S., W. P. Gouveia, and D. H. Johnston, 2003, On the inversion of time-lapse seismic data: 73rd Annual International Meeting, SEG, Expanded Abstracts, 1489–1492.

Schuster, G. T., and A. Quintus-Bosz, 1993, Wavepath eikonal traveltime inversion: Theory: Geophysics, **58**, 1314–1323.

Sheehan, J. R., W. E. Doll, and W. E. Mandell, 2005a, An evaluation of methods and available software for seismic refraction tomography analysis: Journal of Environmental and Engineering Geophysics, **10,** 21–24.

Sheehan, J., W. Doll, D. Watson, and W. Mandell, 2005b, Applications of seismic refraction tomography to karst cavities: US Geological Survey Karst Interest Group Proceedings, 29–38.

Solomon, D. K., G. K. Moore, L. E. Toran, R. B. Dreir, and W. M. McMaster, 1992, Status report: A hydrologic framework for the Oak Ridge Reservation: Environmental Science Division Publication, no. 3815, ORNL/TM-12026.

U.S. Department of Energy (US DOE), 1997, Report on the remedial investigation of Bear Creek Valley at the Oak

Ridge Y-12 Plant, Oak Ridge, Tennessee: DOE/OR/01-1455/V1&D2.

Watson, D. B., W. E. Doll, T. J. Gamey, J. R. Sheehan, and P. M. Jardine, 2005, Plume and lithologic profiling with surface resistivity and seismic tomography: Ground Water, **43**, 169–177.

Zelt, C. A., A. Azaria, and A. Levander, 2006, 3D seismic refraction traveltime tomography at a groundwater contamination site: Geophysics, **71**, no. 5, H67–H78.

Zhao, D., S. Horiuchi, and A. Hasegawa, 1992, Seismic velocity structure of the crust beneath the Japan Islands: Tectonophysics, **212**, 289–301.

Zollo, A., L. D'Auria, R. De Matteis, A. Herrero, J. Virieux, and P. Gasparini, 2002, Bayesian estimation of 2D P-velocity models from active seismic arrival time data: Imaging of the shallow structure of Mt. Vesuvius (Southern Italy): Geophysical Journal International, **151**, 566–582.